Journal of Materials Research and Technology 29 (2024) 5620–5632

Contents lists available at ScienceDirect

Journal of Materials Research and Technology

journal homepage: www.elsevier.com/locate/jmrt

The effects of heat treatment and surface state on the corrosion resistance of laser powder bed fusion 304L stainless steel in 3.5 wt% NaCl solution

Shihao Zhang [a,1], Mengyao Jia [a,1,2], Wei Wang [b], Juan Hou [c], Wenjun Kuang [a,*]

[a] Center for Advancing Materials Performance from the Nanoscale (CAMP-Nano), State Key Laboratory for Mechanical Behavior of Materials, Xi'an Jiaotong University, Xi'an, 710049, PR China
[b] State Key Laboratory for Mechanical Behavior of Materials, Xi'an Jiaotong University, Xi'an, 710049, PR China
[c] School of Materials Science and Chemistry, University of Shanghai for Science and Technology, Shanghai, 200093, PR China

ARTICLE INFO

Handling editor: L Murr

Keywords:
Laser powder bed fusion
304L stainless steel
Corrosion resistance
Heat treatment
Surface state

ABSTRACT

The corrosion resistance of laser powder bed fusion (LPBF) 304L stainless steel (SS) in 3.5 wt% NaCl solution was evaluated at room temperature through potentiodynamic polarization and electrochemical impedance spectroscopy tests. For electropolished samples, annealing at 1200 °C slightly enhanced the corrosion resistance due to changes in crystal orientation and inclusion composition, and reduced residual strain. In contrast, annealing at 1050 °C significantly reduced the corrosion resistance mainly due to the disappearance of dislocation cells and the remained residual dislocations. Residual stress/strain and martensitic transformation induced by sandpaper grinding can also deteriorate the corrosion resistance. Only the as-received sample shows stable passivation regardless of the surface conditions.

1. Introduction

Additive manufacturing, also known as 3D printing, has been developed rapidly in the past two decades. Compared with traditional manufacturing methods, 3D printing has many advantages, including high material utilization rate, short processing cycles and high production efficiency [1]. With the increasing demand for structural complexity of various components, the application opportunities of 3D printing in aerospace, medical, military and other fields have significantly increased [2–7]. Stainless steel (SS) is a widely used material thanks to its good corrosion resistance and mechanical properties. It is desirable to fabricate complex SS components using 3D printing, as this technique can significantly reduce cutting and other processing procedures and shorten the manufacturing cycles. However, it should be noted that the rapid heating and cooling during the manufacturing process can cause 3D printed materials to form microstructures different from the conventional wrought materials, which inevitably affects the properties of the printed materials [8–10]. Given that good corrosion resistance is a key feature of SS, it is necessary to evaluate the corrosion behavior of 3D printed SS and determine the correlation between the corrosion resistance and the microstructure features imparted by this manufacturing technique.

In recent years, some studies have been conducted on the corrosion resistance of 3D printed metallic materials. Kong et al. [11] found that the corrosion resistance of 3D printed 316L SS decreases due to the widespread pores, which leads to localized acidification and aggressive ion enrichment inside the pores. Cellular dislocation is a characteristic microstructure feature of 3D printed materials [12]. It has been reported that the enhanced passivity of laser powder bed fusion (LPBF) 316L SS is due to the electrical potential difference between the cellular boundary and the cellular interior, which leads to the micro-galvanic coupling effect that drives rapid growth of the intracellular passive film [12–14]. Chao et al. [15] found that the typical MnS inclusions in wrought 316L SS no longer exist in LPBF 316L SS, but are replaced by nano-scale inclusions of manganese oxide and silicon oxide. Thus, Cr depletion around MnS can be eliminated and the passivation performance is enhanced via LPBF compared with the wrought counterparts. However, Ettefagh et al. [16] found that due to the presence of residual stress in LPBF 316L SS, the martensite in the stressed zones can be easily corroded and acts as the anodic region, promoting localized corrosion. In addition, different cooling rates in different directions can lead to microstructural anisotropy during printing [17,18], resulting in

* Corresponding author.
E-mail address: wjkuang66@gmail.com (W. Kuang).
[1] These authors have contributed equally to this work.
[2] Present address: School of Materials Science and Engineering, Tsinghua University, Beijing 100084, P. R. China.

https://doi.org/10.1016/j.jmrt.2024.03.025
Received 24 January 2024; Received in revised form 3 March 2024; Accepted 4 March 2024
Available online 8 March 2024

anisotropic corrosion behavior [19–21].

Due to the differences in manufacturing processes, the same type of SS printed in different laboratories often shows different microstructural features, inevitably leading to different properties. Therefore, the printed SS should be evaluated case by case. Due to the potential use of LPBF 304L SS in a broad range of fields including nuclear industry [22], investigating its corrosion resistance is imperative [23–25]. Heat treatment is normally used to tune the as-printed microstructure [26,27], but the impact of such microstructure change on the corrosion resistance has not been unanimously recognized [28,29]. Meanwhile, the surface conditions of the material can also affect its corrosion performance and should be taken into consideration [30,31]. In addition, grinding and electropolishing (EP) are commonly used to reduce the surface roughness of AM parts. Currently, there are many reports on the corrosion performance of sandpaper-ground AM samples [11,15], but the impact of electropolishing on the corrosion performance is still unclear. In this work, the corrosion resistance of LPBF 304L SS was evaluated through potentiodynamic polarization and electrochemical impedance spectroscopy (EIS) tests in NaCl 3.5 wt% (0.6 M) solution at room temperature. The influences of heat treatment and surface state on the passivation behavior of the material were investigated. The evolution in microstructure of the LPBF 304L SS was characterized and the chemical composition of the passive film was analyzed. The corrosion resistance of LPBF 304L SS was discussed with respect to the microstructure features.

2. Experimental details

2.1. Sample preparation

The LPBF 304L SS studied in this work was provided by the Centre for Additive Manufacturing, University of Shanghai for Science and Technology. The powder particle size ranged from 10 μm to 53 μm. A LPBF 304L SS block with a relative density greater than 99.9% was produced by an EOS M290 machine (220W, 40 μm layer thickness, 1.2 m/s scan speed) [3]. The oxygen content was controlled below 2000 ppm under the protection of argon gas. The chemical composition of the as-received LPBF 304L SS was measured by Inductively Coupled Clasma Atomic Emission Spectrometry (ICP-AES) and given in Table 1. The LPBF 304L SS has lower Si (0.065 wt%) and Mn (0.054 wt%) contents but higher Mo (0.83 wt%) content compared to conventional 304/304L SS [10].

In addition to the as-received state, two small rods (with a height of 70 mm and a diameter of ~12 mm) were cut from the LPBF 304L SS block, annealed at 1050 °C and 1200 °C for 0.5 h respectively, and then water quenched. 1050 °C/0.5 h was selected to remove the dislocation cell. 1200 °C heat treatment was used to produce an annealed microstructure. Therefore, comparing the corrosion behavior of these samples helps to distinguish the role of different microstructure features in corrosion. These samples were machined into small cylindrical electrodes for electrochemical test. The studied surface was perpendicular to the building direction, i.e. the x-y plane. The studied surfaces were ground via SiC sandpaper up to 2000-grit, as with previous works [17,32]. Some of the samples were further electropolished at room temperature in 10% (volume fraction) perchloric acid in ethanol at a voltage of 35 V for 30 s to remove the surface hardened layer. Electropolished samples are often used to test the intrinsic corrosion performance of materials [10]. Then a copper wire was soldered on the back of sample. Finally, the untested surfaces of the electrode were insulated with light-curing resins.

2.2. Microstructural characterization

The microstructures of LPBF 304L SSs were examined by Scanning Electron Microscope (SEM), (Scanning) Transmission Electron Microscopy ((S)TEM) and optical microscope (OM). SEM analysis was conducted at 15 kV using a FEI Verios 460 SEM with secondary electron (SE) and backscattered electron (BSE) detectors. The average inclusion size was measured using the image processing software Image J. Four areas of each sample were examined at a magnification of 25000X. The morphological features of the corrosion pits on the surfaces of LPBF 304L SSs after potentiodynamic polarization test were also analyzed. The dislocation structure and inclusions were characterized at 200 kV using a JEM-2100F S/TEM. STEM energy dispersive X-ray spectroscopy (EDS) analysis (with a spot diameter of 0.7 nm) was carried out on multiple inclusions for each sample.

Electron back-scattered diffraction (EBSD) used for evaluating the residual strain was performed in a FEI Helios 600 SEM equipped with an Oxford Nordlays EBSD detector. The EBSD analysis was conducted with a step size of 0.5 μm and a working distance of 8.5 mm. Kernel Average Misorientation (KAM) maps were used to qualitatively assess the local residual plastic strain. A KAM map shows the mean value of the misorientations between a point and its neighboring points. The KAM values were determined from an 11 × 11 kernel (Channel5, Oxford). The average grain size and texture inverse pole figure of each sample were obtained from EBSD data, sampled from an area of 200 × 250 μm^2.

X-ray diffraction (XRD) measurements were performed to identify the phase of LPBF 304L SSs, using a Bruker D8 ADVANCE equipment. The diffraction angle 2θ was scanned from 20° to 100°, with a step size of 0.02° and a scanning rate of $12°\cdot min^{-1}$.

The porosity analysis was performed per ASTM E2109. Porosity analysis was conducted on the polished surface (with a sampling area greater than 40 mm^2) using a ZEISS Axio Scope.A1 optical microscope with a relatively large field of view which can provide significant contrast between the matrix and pores. Area percentage of pores was determined by measuring the area of the exposed pores. Only large pores (diameter >5 μm) were counted because of the resolution limit of OM and the small pore had little effect on pitting [33]. The uncertainty of the area percentage of pores and the mean pore size was evaluated via standard deviations.

To measure the surface topography and roughness of the samples, an OLS5100 laser scanning confocal microscope was used on both the electropolished and 2000# sandpaper-ground samples.

2.3. Micro-hardness tests

The intrinsic hardness of samples was determined through micro-hardness testing on the electropolished sample (the surface hardened layer was removed by electropolishing). The micro-hardness tests were performed using an HXD-1000TMC/LCD micro-hardness tester with a load of 200 g and a holding time of 15 s based on ASTM E384. At least 10 evenly distributed hardness indentations were made on each sample and the mean value was obtained.

2.4. Electrochemical tests

Potentiodynamic polarization and EIS tests were conducted in a 3.5 wt% NaCl solution at room temperature using a Gamry Reference 600+ electrochemical workstation. In this work, saturated calomel electrode (SCE) was used as a reference electrode. The potentials in this paper, if not specified, were all relative to the reference electrode. A 15 mm × 15

Table 1
Chemical compositions (wt. %) of LPBF 304L SS.

Material	C	N	Si	Mn	P	S	Cr	Ni	Mo	O	Fe
LPBF 304L	0.014	0.013	0.065	0.054	0.027	0.003	19.07	9.62	0.83	0.031	Bal

mm Pt sheet was used as a counter electrode, and the insulated sample with an exposed area of ~100 mm^2 was used as the working electrode.

Prior to each electrochemical test, nitrogen gas was purged into the electrochemical cell to remove the dissolved oxygen from the solution, thereby minimizing the interference of the oxygen redox reaction. Open circuit potential (Eoc) was measured to monitor the process of deoxygenation. Normally Eoc was stabilized after purging for 60 min. Then potentiodynamic polarization test was conducted from −0.3 V vs Eoc at a scanning rate of 0.167 mV s^{-1}. The test was stopped manually when the current rapidly increased (indicating pitting corrosion occurred). Nitrogen gas was continuously purged throughout the test. The test for each sample was tested for three times and a representative curve for each condition is presented.

In order to evaluate the performance of the passivation film within the passivation range, EIS testing was conducted on samples that have passivation range, including as-received + EP, as-received + sandpaper ground and 1200 + EP samples. Before conducting the EIS test, the solutions were deoxygenated and the samples were subjected to 1 h of potentiostatic polarization in the passive range to establish a stable passive film. The as-received + EP, as-received + sandpaper ground and 1200 + EP samples were polarized at 0.2, 0.1 and 0.2 V vs. Eref, respectively. The impedance was measured over a frequency range of 10^5 Hz to 10^{-2} Hz as in previous works [34,35], with a perturbation of sinusoidal waveform (10 mV in amplitude). Gamry Echem Analyst software was used for EIS data analysis. Causality and linearity of the impedance was checked via Kramers-Kronig transformation. The goodness of Kramers-Kronig analysis is below $3*10^{-5}$, indicating that the system has reached a steady-state condition.

2.5. XPS measurement

X-ray photoelectron spectroscopy (XPS) was used to measure the chemical composition of passive films formed on LPBF 304L SSs after EIS test. A Thermo Fisher ESCALAB Xi^+ instrument equipped with a monochromatic Al Kα radiation of 1486.68 eV was used for the XPS analysis. Depth sputtering was performed using 2000 eV Ar^+ in a high current mode and the raster width was 2.5 mm. The profiles of Cr, Fe, Ni and O were acquired from the surface of passive films to the interior of matrix.

3. Results

3.1. Original microstructures

The SEM-BSE micrographs of different heat-treated LPBF 304L SSs before electrochemical tests are shown in Fig. 1, and the average grain sizes are listed in Table 2. The tested surface of the sample is the x-y plane. From Fig. 1(a_1, b_1), the grain sizes of the as-received and 1050 °C heat-treated samples are similar (8.0 ± 1.29 μm vs 9.9 ± 1.22 μm). This indicates that the grain size didn't change significantly after the heat-

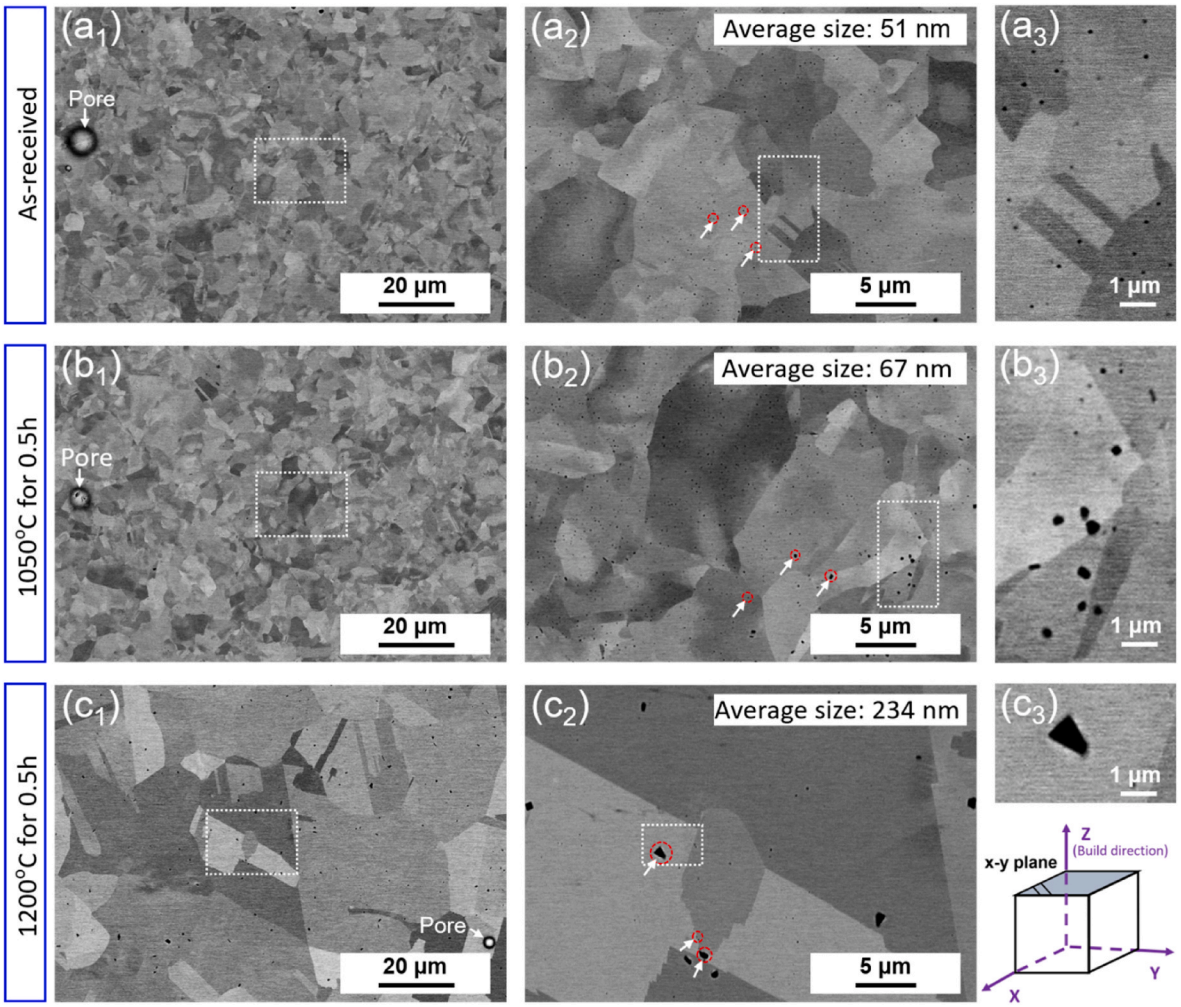

Fig. 1. SEM-BSE images of LPBF 304L SS (x-y plane) under different conditions: (a_1, a_2, a_3) as-received; (b_1, b_2, b_3) 1050 °C heat-treated for 0.5 h; (c_1, c_2, c_3) 1200 °C heat-treated for 0.5 h. The inclusions are marked by the red dashed circle. (For interpretation of the references to colour in this figure legend, the reader is referred to the Web version of this article.)

Table 2
Microstructure characteristics and micro-hardness for as-received, 1050 °C heat-treated and 1200 °C heat-treated samples.

Condition	Average grain size (μm)	Proportion of Σ3 twin boundarie to grain boundary (%)	Average inclusions size (nm)	Micro-hardness (HV)	Area percentage porosity (%)	Mean pore size (μm)
As-received	8.0 ± 1.29	35.5	51 ± 24.2	225.6 ± 8.3	0.041 ± 0.03	18 ± 6.6
1050 °C, 0.5h	9.9 ± 1.22	34.1	67 ± 52.0	205.5 ± 6.3	0.041 ± 0.03	21 ± 5.8
1200 °C, 0.5h	46.9 ± 16.99	60.8	234 ± 194.9	180.1 ± 8.3	0.039 ± 0.02	21 ± 6.5

treatment at 1050 °C. However, the heat-treatment at 1200 °C notably increased the grain size to 46.9 ± 16.99 μm (Fig. 1c_1). The grain morphology changes from fine grains with curly grain boundaries (Fig. 1 (a_2, b_2)) to equiaxed grains with almost straight grain boundaries (Fig. 1 (c_1, c_2)). The average inclusion sizes measured from the SEM images are presented in Table 2. As shown in Fig. 1(a_2, a_3, b_2, b_3), nano-scale spherical inclusions can be observed in both the as-received and 1050 °C heat-treated samples at higher magnifications. Nano-inclusions with higher density and smaller size (average size of 51 nm) are dispersed in the as-received samples, while the sample heat-treated at 1050 °C shows fewer but larger inclusions (average size of 67 nm) (Fig. 1 (a_2, b_2)). Largest inclusions (average size of 234 nm) were observed in the 1200 °C heat-treated samples (Fig. 1(c_1)). The area percentage porosity and mean diameter of pores in LPBF 304L SS with different heat treatment are basically the same (Table 2).

KAM maps overlapped with grain boundary network obtained from three different states of LPBF 304L SSs are shown in Fig. 2(a_1, b_1 and c_1). The grain boundary characteristics and micro-hardness values of three different states of LPBF 304L SSs are also summarized in Table 2. The 1200 °C heat-treated sample exhibits equiaxed coarse grains with 60.8% twin boundaries, which is higher than those of the as-received (35.5%) and 1050 °C heat-treated (34.1%) samples. The TEM characterization of Σ3 twin boundaries are shown in Fig. S1. The average KAM values of the as-received, 1050 °C and 1200 °C heat-treated samples are 0.864, 0.729 and 0.719, respectively, indicating that the residual strain decreases with increasing annealing temperature. The average micro-hardness values of the as-received, 1050 °C and 1200 °C heat-treated samples are 225.6 ± 8.3, 205.5 ± 6.3 and 180.1 ± 8.3 HV, consistent with the decreasing trend of the average KAM values. EBSD characterization reveals an obvious texture in the three types of LPBF 304L SS samples. The <101> crystallographic direction tends to align with the building direction (Fig. 2(d_1-d_3)). As the heat treatment temperature increases, the <101> texture is enhanced.

To characterize the dislocations of different heat-treated LPBF 304L SSs, TEM bright and dark field images were captured (Fig. 3). Fig. 3(a_1) shows that the dislocation cells in the as-received sample are composed of highly entangled dislocations. Fig. 3(b_1) shows that after heat-treatment at 1050 °C, partial recovery occurred and the dislocation density notably decreased with dislocation migration and annihilation. Fig. 3(c_1) shows that after heat-treatment at 1200 °C, the dislocation density further decreases with the increase of dislocation mobility. The chemical compositions of typical inclusions are listed in Table 3. STEM-EDS results show that the morphology (Supplementary materials Fig. S2) and chemical composition of the inclusions of the as-received samples changed after heat-treatments at different temperatures. The inclusions in the as-received sample are mostly spherical Si-rich nano oxide particles with relatively low oxygen content, while some inclusions are slightly Cr-enriched. With the increase in heat-treatment temperature, the morphology of inclusions transforms into polyhedron, and the content of O also increases. When heat-treatment is performed at 1200 °C, the inclusions become rich in Cr (Cr: 51.29 at. %) (Table 3). No MnS inclusions were found under any of the three conditions.

The surface topography of the sample surfaces is shown in Fig. 4. The electropolished sample (Fig. 4a and c) has a relatively smooth surface with a fluctuation about 300 nm over a hundred microns. In contrast, the

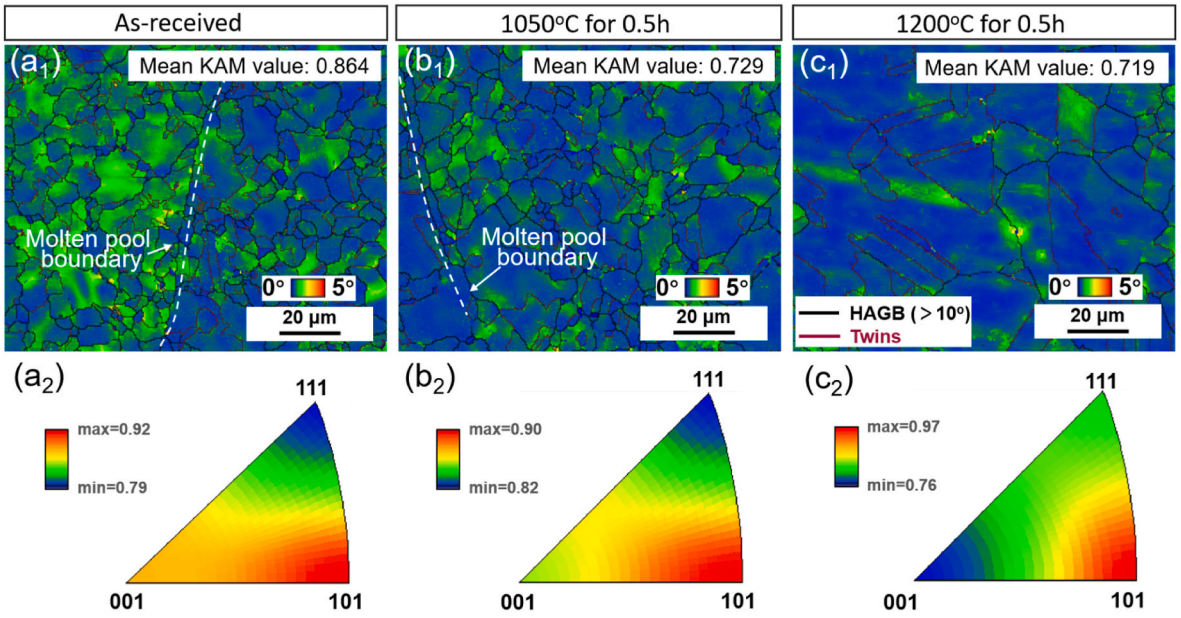

Fig. 2. KAM maps overlapped with grain boundary network of electropolished (a_1) as-received; (b_1) 1050 °C heat-treated; (c_1) 1200 °C heat-treated LPBF 304L SS. The black and red lines represent the grain boundaries with a misorientation angle >10° and 60° < 111> Σ3 twin boundaries, respectively. Texture analysis of LPBF 304L SS in build direction: (a_2) As-received, (b_2) 1050 °C heat-treated and (c_2) 1200 °C heat-treated samples. (For interpretation of the references to colour in this figure legend, the reader is referred to the Web version of this article.)

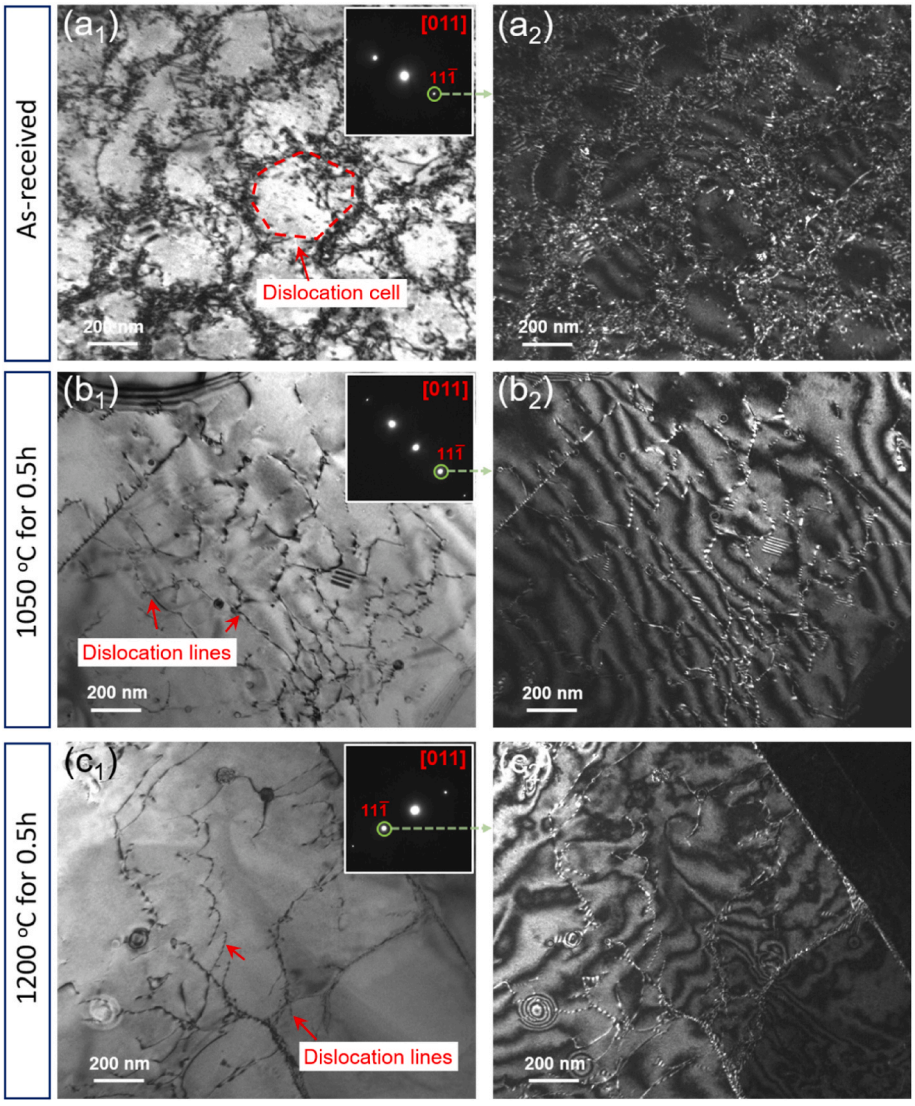

Fig. 3. TEM two-beam bright and dark field imaging of dislocations: (a_1, a_2) As-received, (b_1, b_2) 1050 °C heat-treated and (c_1, c_2) 1200 °C heat-treated samples.

Table 3
The STEM-EDS results (at.%) of inclusions of As-received, 1050 °C heat-treated and 1200 °C heat-treated samples.

Condition	Type	O K	Si K	Cr K	Mn K	Fe K	Ni K	Mo K
As-received	Si-rich	29.99	5.26	17.54	0.29	39.75	6.67	0.50
	Si–Cr-rich	8.27	1.98	24.98	0.15	57.65	6.53	0.43
1050 °C, 0.5h	Cr-rich	44.38	0.20	37.33	0.07	15.99	1.95	0.02
	Fe–Cr-rich	25.01	1.02	26.64	2.69	39.49	4.73	0.43
1200 °C, 0.5h	Cr-rich	46.00	0.08	51.29	0.17	2.23	0.21	0.02

surface of the sandpaper-ground sample (Fig. 4b and c) is not smooth at the micrometer scale. The surface roughness and area are quantified with arithmetical mean height of the scale limited surface (Sa) and the developed interfacial area ratio (Sdr). Sdr represents the actual increase in interfacial area relative to the projected area of the interface. The surface roughness Ra and the developed interfacial area ratio Sdr of these two samples are very similar. The low Sdr value suggests that neither surface treatment significantly increased the surface area of the samples.

XRD patterns obtained from the as-received and two heat-treated LPBF 304L SSs with different surface conditions are shown in Fig. 5. The peaks correspond to either austenite or martensite. All the electropolished samples only show austenite peaks. Comparing the XRD results of three electropolished samples, it can be found that the relative intensity of the γ (220) peak (using the intensity of the (111) peak as a reference) significantly increased in the heat-treated samples (Fig. 5a). The relative intensity of the γ (220) increases from 0.395 to 0.540, and then to 0.758. From the partial enlarged spectrum on the right side of Fig. 5a, it can be seen that with the increase of temperature, the (220) peak intensity becomes higher and the peak width becomes narrower, indicating that the grain orientation of the material is changed and the residual stress is decreased. The sandpaper-ground samples (Fig. 5b) have a weak martensite peak near the austenite peak γ (111), suggesting that the transformation of γ austenite to α′ martensite occurred on the surface during the grinding. From the enlarged spectrum of Fig. 5b, the 1200 °C heat-treated sample has a relatively stronger peak of α’

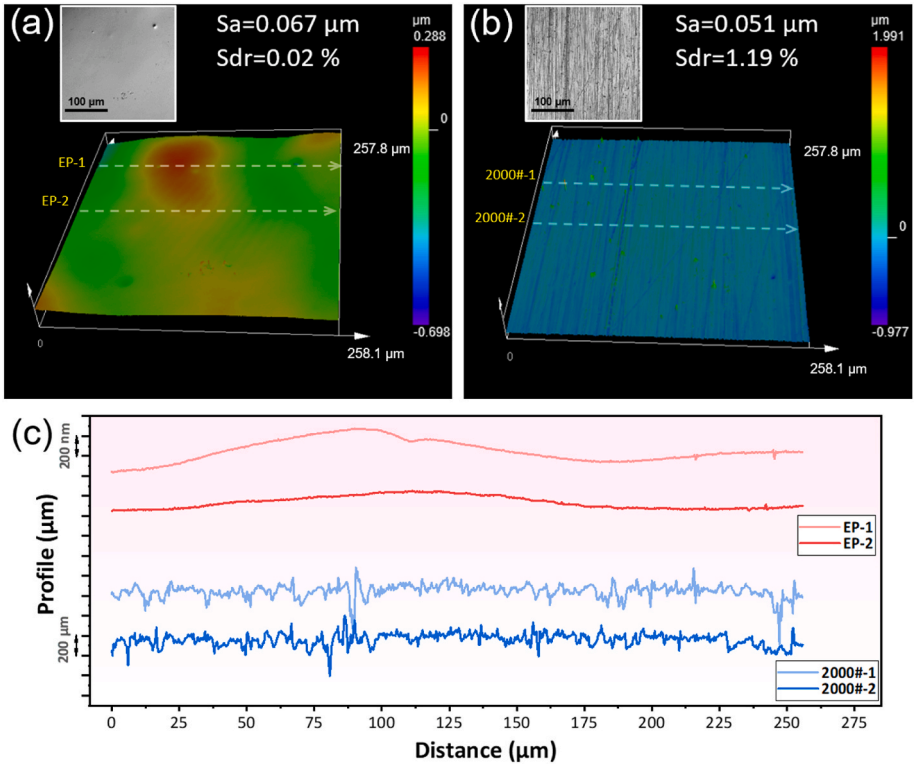

Fig. 4. The surface topography of the (a) electropolished sample and (b) 2000# sandpaper-ground sample. (c) Two-dimensional height profiles along the dash lines in a and b.

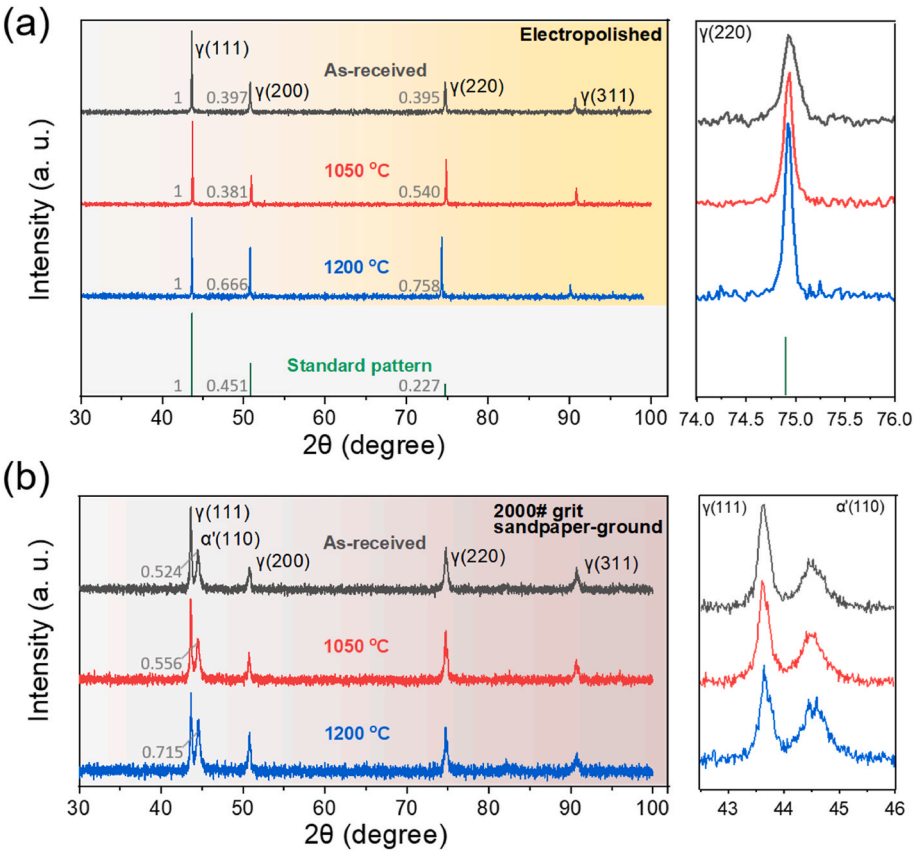

Fig. 5. XRD patterns of (a) electropolished and (b) 2000# grit sandpaper-ground LPBF 304L stainless steel. The standard pattern of γ-iron is shown on the bottom of a. The relative intensity values of some peaks are listed on the left side of their respective peak. α′ martensite and α ferrite phases show similar peaks in XRD.

martensite (0.715 vs 0.524 and 0.556). The background noise is mainly caused by the high residual stress introduced on the sample surface during the sandpaper grinding process.

3.2. Results of electrochemical tests

Fig. 6 shows the potentiodynamic polarization curves of the as-received and heat-treated LPBF 304L SSs in a 3.5 wt% NaCl solution at room temperature. The sample surfaces were all electropolished. Each sample was tested three times, and one representative curve for each condition is shown here. From the curves, it can be seen that the as-received LPBF 304L SS and the 1200 °C heat-treated samples show a broad passivation range, indicating that they both possess good corrosion resistance. Unexpectedly, the 1050 °C heat-treated samples show no clear passivation range. The passivation range is defined as the potential range with low anodic current density (normally below 1 μA/cm^2) and barely changes, as shown in Fig. 6.

In addition, the Tafel ranges of the polarization curves were fitted to obtain the corrosion current of each sample. The fitting results and the average width of the passivation range are listed in Table 4. Table 4 shows that compared to 1050 °C heat-treated sample, the as-received and 1200 °C heat-treated samples have relatively lower corrosion current and wider passive ranges. And they show comparable corrosion currents and widths of passivation range, although the 1200 °C heat-treated sample exhibits larger variation. The 1050 °C heat-treated samples can hardly be passivated.

In order to investigate the effect of surface state on corrosion behavior, the potentiodynamic polarization curves of sample surfaces after electropolished and sandpaper ground (2000# grit) were measured on samples heat-treated under different conditions. The results are shown in Fig. 7 and Table 4. From the curves, it can be seen that the electropolished samples all exhibit better corrosion resistance than their sandpaper-ground counterparts. Specifically, the corrosion currents of the electropolished samples are all lower than samples ground with sandpapers, and the passive ranges are also wider for the electropolished samples. It should be noted that for the sandpaper-ground surface condition, only the as-received sample shows stable passivation and much lower corrosion current density than the other two thermally treated samples.

After potentiodynamic polarization tests, the surfaces of the electropolished samples were examined by OM (Supplementary materials Fig. S3) and SEM (Fig. 8). Fig. S3 shows the appearance of surface pitting after polarization tests. Due to the lack of stable passivation, the 1050 °C heat-treated sample shows the most corrosion pits. Fig. 8(a_1, b_1 and c_1) show similar morphology of pits on the three samples at low magnification. At higher magnification, the cellular sub-structures are observed at the bottom of the corrosion pits of the as-received LPBF 304L SS (Fig. 8a_2). The average cell diameter is about 500 nm. As depicted in Fig. 8(b_2 and c_2), the cellular structure disappeared after the heat treatments. In addition, almost no inclusions can be seen in the pits of the as-received or the 1050 °C heat-treated samples, which may be attributed to the dissolution or shedding of inclusions. The 1200 °C heat-treated sample maintains the same inclusion density as its original microstructure at the bottom of the corrosion pits (Fig. 1(c_1, c_2)).

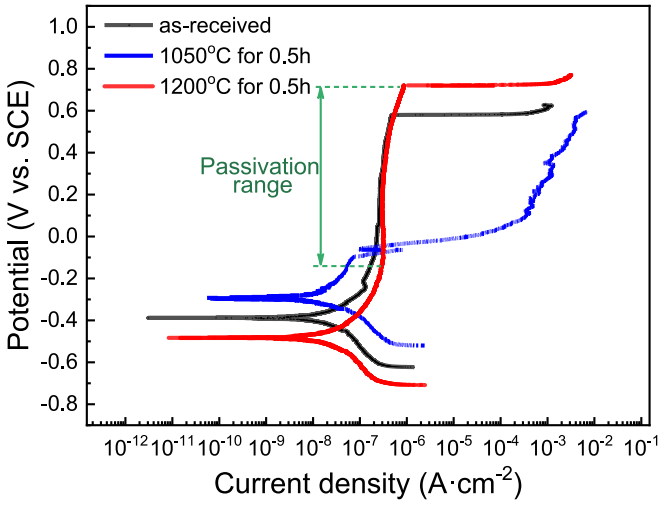

Fig. 6. Potentiodynamic polarization curves of the as-received and two heat-treated LPBF 304L SS samples in 3.5 wt% NaCl solution at room temperature, with a scan rate of 0.167 mV s^{-1}. The sample surfaces were electropolished.

Table 4
Tafel fitting results and passive ranges obtained from the potentiodynamic polarization curves.

Condition	Suface state	Corrosion current density (nA·cm^{-2})	Passive range width (mV)
As-received	Electreopolished	21.2 ± 7.6	543.3 ± 112.0
	Sandpaper ground	64.5 ± 9.8	373.1 ± 79.7
1050 °C, 0.5h	Electreopolished	117.1 ± 64.9	/
	Sandpaper ground	224.3 ± 10.3	/
1200 °C, 0.5h	Electreopolished	23.2 ± 12.5	648.9 ± 366.8
	Sandpaper ground	1610.7 ± 1040.8	/

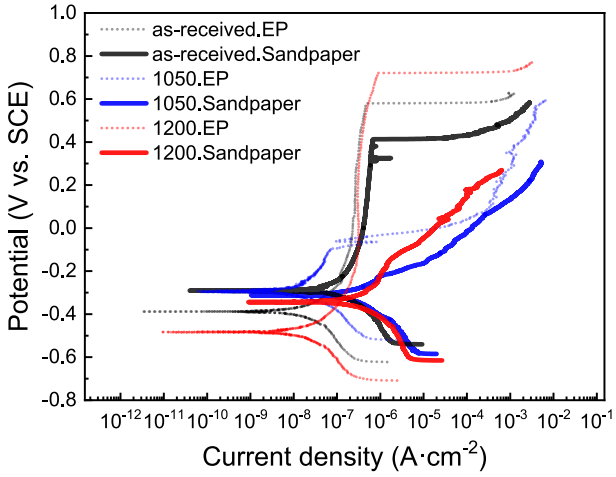

Fig. 7. Potentiodynamic polarization curves of LPBF 304L SS samples with different surface states in 3.5 wt% NaCl solution at room temperature, with a scan rate of 0.167 mV s^{-1}. (EP- electropolished).

As shown in the potentiodynamic polarization curves (Figs. 6 and 7), only the as-received samples and 1200 °C heat-treated sample with electropolished surfaces can be passivated in 3.5 wt% NaCl solution at room temperature. Fig. 9 displays the EIS results from these samples. The Nyquist plots (Fig. 9a) for the three samples demonstrate the partial capacitive semicircles. The 1200.EP sample shows the largest arc radius, followed by as-received.EP and as-received.sandpaper sample. The equivalent circuit (as shown in Fig. 9c) was used to fit the EIS data. The electrical equivalent circuit consists of a solution resistance (R_s), a charge transfer resistance (R_t), and a constant phase element (CPE). The CPE can be interpreted as a capacitor with non-ideal properties, and its impedance can be expressed as:

$$Z = \frac{1}{Q_0}(j\omega)^{-n}$$

Where Q_0 represent CPE amplitude; j represent imaginary unit; ω represent angular frequency; n is the depression coefficient ($0 < n < 1$).

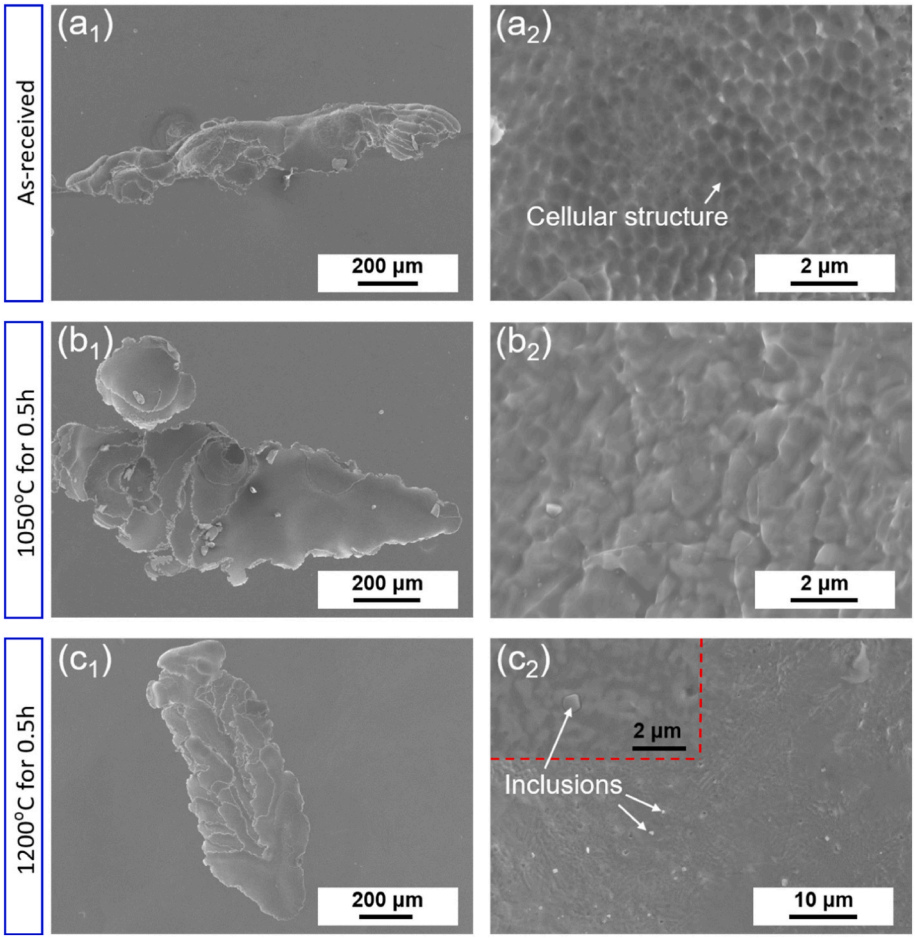

Fig. 8. SEM micrographs of electropolished sample surfaces after the polarization test (current density: 1–10 A cm^{-2}): (a_1, a_2) as-received, (b_1, b_2) heat-treated at 1050 °C for 0.5 h and (c_1, c_2) heat-treated at 1200 °C for 0.5 h.

The fitting results of EIS data are listed in Table 5. The goodness of the fitting is on the order of 10^{-4}, which suggests good consistency between the experimental results and the equivalent circuit model.

As shown in Fig. 9, the electropolished 1200 °C heat-treated sample shows the highest impedance, followed by the electropolished as-received sample, and then the sandpaper-ground as-received sample. As listed in Table 5, the passive film formed on the electropolished 1200 °C heat-treated sample has the highest charge transfer resistance, while the sandpaper-ground as-received sample has the lowest. Therefore, for the electropolished surface state, the passive film formed on 1200 °C heat-treated sample is more protective than that on the as-received counterpart. For the as-received LPBF 304L SS, the electropolished sample shows slightly higher corrosion resistance than the sandpaper-ground sample.

3.3. The chemical composition of passive film

The depth profiles (in wt. %) of the main elements (Fe, Cr, Ni, O) in the passive films were measured using XPS, as shown in Fig. 10. All the profiles show the enrichment of Cr and the depletion of Fe and Ni in the passive films. Fig. 10d shows the Cr profiles in the passive films of different LPBF 304L SSs. It is found that the maximum Cr concentration is comparable between these two electropolished samples, which is significantly higher than that of the ground sample (34 wt% vs. 26 wt%). The thickness of the passive film can be estimated from the O profile which roughly corresponds to the depth where the O content drops to half. The estimated film thicknesses based on the oxygen profile and the sputtering rate (0.24 nm/s, based on Ta_2O_5) are as follows: 3.12 nm for sandpaper ground as-received sample, 4.93 nm for electropolished as-received sample and 8.25 nm for electropolished 1200 °C heat-treated sample. Therefore, the electropolished 1200 °C heat-treated sample has the thickest passive film, followed by the electropolished as-received sample, and then the sandpaper ground as-received sample.

3.4. Summary of the electrochemical properties

According to the potentiodynamic polarization curves (Figs. 6 and 7) and Tafel fitting results (Table 4), the order of decrease in corrosion resistance for the electropolished samples is 1200 °C heat-treated LPBF 304L SS, the as-received sample, and finally the 1050 °C heat-treated sample. However, for the sandpaper-ground surface state, the as-received sample shows the highest corrosion resistance while the other two samples can not be passivated. Under the same heat treatment condition, the electropolished samples all show better corrosion resistance than their sandpaper-ground counterparts. The results of the EIS tests (Fig. 9, Table 5) exhibit a consistent trend, indicating that the passive film of the electropolished 1200 °C heat-treated sample has the best performance, followed by the electropolished as-received counterpart, and finally the sandpaper-ground as-received sample.

4. Discussion

One of the novel aspects of this study is the use of electropolishing as a sample preparation process, which is also commonly used in the additive manufacturing industry to process various parts [36]. Electropolishing can greatly avoid the microstructure changes caused by the

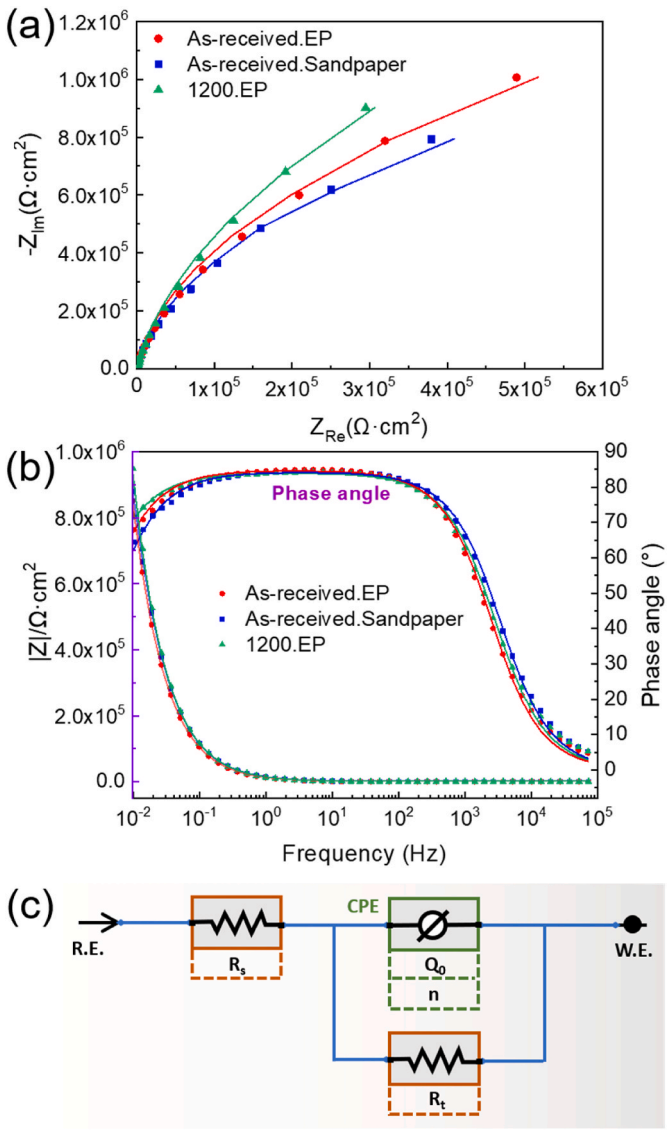

Fig. 9. EIS results for electropolished as-received, sandpaper-ground as-received and electropolished 1200 °C heat-treated LPBF 304L SS in 3.5 wt% NaCl solution at room temperature: (a) Nyquist plots; (b) Bode plots (The fitting lines are represented in solid lines. ep-electropolished); (c) equivalent circuit for data fitting.

sandpaper-grinding process, including grain refinement, deformation induced martensite, twinning, and increased dislocation density [31, 37–39], enabling a more accurate assessment of the material's corrosion behavior. In this study, the electropolished samples were used to investigate the effect of heat treatment on corrosion behavior. Additionally, the influence of two surface states, i.e., electropolishing and sandpaper grinding, on corrosion behavior was also examined. The effects of heat treatment and surface state on corrosion resistance will be discussed separately below.

4.1. Effects of annealing treatment on the corrosion resistance of LPBF SS

Changes in microstructure after heat-treatment are responsible for the changes in the corrosion resistance of LPBF 304L SS. Compared with the as-received sample, the 1050 °C heat-treated one has a comparable grain size but reduced residual strain (Fig. 2). More importantly, the dislocation cells disappeared after heat treatment. Dislocation cells are composed of entangled dislocations, and there is a small amount of elements with high melting point (such as Mo or Cr) segregate at the dislocation cell wall [12,40]. High density of dislocations can increase the reactivity and diffusivity of elements [41]. During the passivation process, the dislocation cells can promote the formation of the compact film, as it was found that the dislocation cells can provide more sites for passive film nucleation. Kong et al. [27] found that LPBF 316L SS with dislocation cells can form a thicker passive film than the wrought 316L SS in a 0.04 M borate buffer solution. They proposed that the chemical heterogeneity near the dislocation cells can induce micro-galvanic couple which accelerates the formation of stable passive film on LPBF 316L SS. Consistently, Man et al. [42] proposed that sub-grain boundaries and dislocations in LPBF 316L SS promote the formation of passive film in a simulated body fluid. Thus, the absence of dislocation cell impairs the passivation ability of 1050 °C heat-treated sample, and there is no stable passivation range for this material (Fig. 6). Despite the largely diminished dislocation cells, there are still some dislocations and residual strain remained in the 1050 °C heat-treated sample (Figs. 2 and 3). The density of these remnant dislocations is not sufficient to promote passivation as in the as-received sample, but it may be detrimental to the corrosion resistance of sample as the remnant dislocations may induce a more defective passive film. Consistently, it has been widely reported that the dislocation pile up caused by cold working can lead to degradation of the corrosion resistance of stainless steels [43–46].

When the heat treatment temperature was increased to 1200 °C, the material was completely recrystallized. Compared with the as-received and the 1050 °C heat-treated samples, both the grain size of the 1200 °C heat-treated sample and inclusion size increase, and the grains become equiaxed. In addition, the {101} texture is further enhanced, and the residual strain is further reduced (Fig. 2). The higher pitting potential, broader passivation range and higher impedance values of the 1200 °C heat-treated sample (Fig. 6, Tables 4 and 5) suggest that the microstructure changes induced by the 1200 °C annealing result in higher corrosion resistance.

The further reduced residual strain in the 1200 °C heat-treated sample would help to enhance the corrosion resistance of material as the dislocation pile ups were further relieved. The grain orientation also plays a role. The as-received sample exhibits a <101> crystallographic texture due to preferential grain growth along the building direction, which has also been reported in some LPBF SSs [21]. After 1200 °C heat treatment (Fig. 5), both the relative intensities of γ (200) and γ (220) become higher than those of the non-textured γ PDF card (standard pattern) [47]. Moreover, the intensity of (220) peak increases more significantly (from 0.227 to 0.758) than that of (200) peak (from 0.451 to 0.666). The {101} texture was significantly enhanced after 1200 °C heat treatment. Previous studies [48] have shown that the crystallographic planes that close to {101} or {111} have higher pitting resistance compared with those close to {100} orientation. Kong et al. [32] proposed that more γ (101) grains on the surface of LPBF 316L SS after heat treatment can improve its corrosion resistance. Thus, the increase of the {101} oriented crystal plane may be an important factor in

Table 5
Impedance parameters through equivalent circuits fitting for three samples with passivation ranges.

Condition	Surface state	R_s (Ω·cm^2)	R_t (10^6 Ω cm^2)	Q_0 (10^{-6} Ω^{-1}·s^n·cm^{-2})	n	Goodness (10^{-6})
As-received	Sandpaper ground	6.58	2.36	13.43	0.94	644.1
	Electropolished	7.52	2.83	14.85	0.94	779.2
1200 °C, 0.5h	Electropolished	7.92	4.13	13.38	0.93	782.8

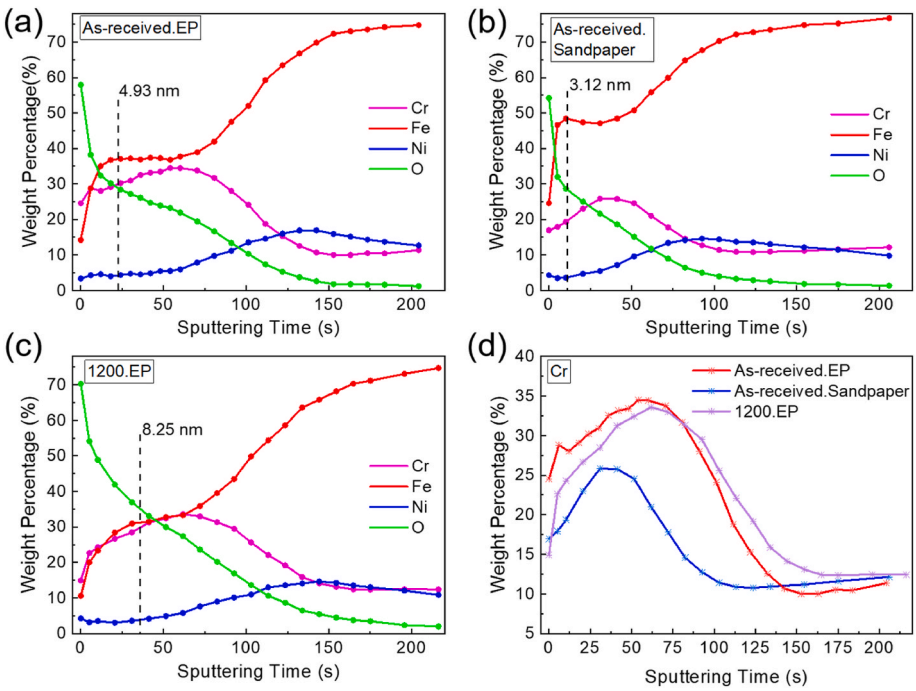

Fig. 10. The XPS depth profiles of passive films formed on LPBF 304L SS: (a) electropolished as-received; (b) sandpaper-ground as-received; (c) electropolished 1200 °C heat-treated; (d) The depth profiles of Cr.

improving the corrosion resistance of 1200 °C heat-treated sample.

The inclusion may also play an important role in the corrosion behavior of LPBF SS [49]. However, most of the existing electrochemical results of LPBF SS focus on materials with conventional chemical compositions, which usually contain more than 0.1 wt% Si and Mn [50,51]. There are numerous studies showing that inclusions tend to change (such as changes in size, composition, and distribution) with the increase of heat treatment temperature [52,53]. However, limited work has been done to study the effects of changes in inclusions on the corrosion resistance of LPBF SS. Laleh et al. [29] found that the pitting corrosion resistance of LPBF 316L SS (0.56 wt% Si and 1.11 wt% Mn) decreased drastically after thermal treated at temperatures above 1000 °C, which was due to the formation of detrimental MnS inclusions. In this work, the Si and Mn contents of LPBF 304L SS (containing 0.065 wt% Si and 0.054 wt% Mn) are lower than those of other SSs in the literature [50,54]. Therefore, the chemical composition of inclusions in this LPBF 304L SS is quite different from those in previous LPBF SS, as listed in Table 3. The inclusions in the as-received sample are Si-riched oxides. Previous studies have reported that Si can also exist in the form of silicates [55–57]. Prismatic-shaped inclusions are found in the two heat-treated samples (Fig. S2), which are confirmed to be mainly Cr-rich oxides, consistent with other reports [52,54]. Zhang et al. investigated the corrosion behavior of inclusion of LPBF 316L SS in $FeCl_3$ solution and found that the Mn–Si-rich (manganese silicate) inclusions are prone to anodic dissolution [58]. Silicates are chemically and structurally different from typical protective passive films that naturally form on the sample surface. These silicates may also impede the formation of natural passivation films, thus leading to localized corrosion when samples are exposed to corrosive environments [59]. However, the inclusion size is small and the density is high, making the corrosion quite uniform on the sample surface and no stable pit remains. That may be why the LPBF SS shows a stable passive range. For the heat-treated samples, although the inclusion size increases, the inclusion becomes enriched in Cr which is close to the chemical composition of stable passive film. Such inclusions will not form any galvanic couples with the surrounding matrix once passive film forms elsewhere. Thus, the 1200 °C heat-treated sample can also form stable passive films.

Grain size should also be considered as one of the vital factors influencing the corrosion behavior. The 1050 °C and 1200 °C heat-treated samples have different grain sizes (9.9 ± 1.22 vs 46.9 ± 16.99 μm). However, the influence of grain size on corrosion resistance is still controversial at present, even for the same alloy [30,60,61]. Ralston et al. [60] proposed that if an electrolyte elicits active behavior from a course-grained sample, then grain refinement tends to make the surface "more" active and enhances corrosion. Conversely, if a coarse-grained microstructure is passive in a given electrolyte, then finer grain results in an even more stable passive film. In this work, coarse-grained 1200 °C heat-treated sample exhibits a good passivation behavior. Thus, refining the grain is more likely to enhance the passivation ability of this material. Nevertheless, the LPBF SS doesn't show higher corrosion resistance than the 1200 °C heat-treated sample, which may probably due to the conflicting effects of other factors mentioned above.

Overall, the good corrosion resistance of as-received samples is mainly due to the presence of dislocation cells, consistent with previous findings [12,17]. However, the effect of heat treatment on corrosion resistance in LPBF 304L SS differs from that observed in conventional AM SSs. For conventional AM SSs, formation of Si/Mn-rich inclusions and annihilation of cellular dislocations normally occur during heat treatment, resulting in reduced corrosion resistance [55,62]. In contrast, this LPBF 304L SS behaves differently. At 1050 °C, the disappearance of dislocation cells leads to residual dislocations and strain, diminishing the passivation ability. Conversely, heat treatment at 1200 °C results in reduced residual dislocations and strain, grain growth, formation of Cr-rich inclusion and enhanced {101} texture, thus effectively enhancing the corrosion resistance.

4.2. *Effects of surface state on corrosion resistance*

Surface state plays a critical role in determining the corrosion properties of materials, as it affects the microstructure and topography of materials that comes into direct contact with the corrosive medium. As mentioned in Section 4.1, the electropolished samples were used to study the influence of intrinsic microstructure on corrosion behavior. In this section, the corrosion behavior of samples with electropolished and

2000# sandpaper-ground surfaces is compared, and the influence of surface state on corrosion resistance is discussed.

During the grinding process, when the hard particles on the sandpaper come in contact with the sample surface, the surface of the material will be subjected to simultaneous interaction of compressive stress and shearing force, resulting in a change in surface roughness. Due to the complex stress state generated during the grinding process, the surface grains are refined and large residual strain/stress is produced. Strain induced phase transformation can even occur in some materials [63]. These microstructure changes in material can affect the corrosion performance.

In addition to the increased surface roughness, the three sandpaper-ground LPBF 304L SS samples all show feature peaks of α′-martensite (Fig. 5b), indicating that the strain-induced martensite phase transformation occurs on the surface during the grinding process. Compared with the electropolished sample, the XRD spectrum of sandpaper-ground samples shows an increase in the background noise and wider diffraction peaks, which is due to the residual stress generated on the sample surface during grinding [64]. In addition, grinding can also lead to the formation of an ultrafine-grained layer on the sample surface. By assessing the extent of XRD peak broadening of sandpaper-ground samples [65], the grain size of surface ultrafine-grained layer can be roughly estimated to be less than 30 nm. Chang et al. [38] also reported that the 1200# sandpaper-ground surface has a thin ultrafine-grained layer (about 0.2–0.4 μm in thickness). Therefore, the thickness of the ultrafine-grained layer on the sample surface after grinding with the 2000# sandpapers in this work should not be more than 0.4 μm.

The potentiodynamic polarization curves and EIS results also show that for both the as-received and heat-treated LPBF 304L SS samples, the sandpaper-ground surfaces show inferior corrosion resistance than the electropolished counterparts (Figs. 7 and 9). Especially for the 1200 °C heat-treated sample, the sandpaper-ground surface even doesn't show stable passivation range (Fig. 7). Therefore, the corrosion resistance can be significantly degraded by sandpaper grinding due to changes in microstructure. Similarly, Schaller et al. [66] investigated the effect of surface conditions on the corrosion resistance of LPBF 304L SS in 1 M NaCl solution and found that the corrosion resistance decreases with the increase of the mesh number of sandpaper. The surface of sandpaper-ground samples contains a layer of highly deformed ultrafine grains mixed with strain-induced martensite. As mentioned above, grain refinement helps to enhance the corrosion resistance of the material by increasing the stability of the passivation film. But the dislocation piling up due to cold working is detrimental to corrosion resistance. In addition, martensite significantly deteriorates the corrosion performance of materials, which has been confirmed in previous studies. For example, Li et al. [67] studied the effect of strain-induced martensite on the tribo corrosion of 316L SS in artificial seawater, and found that the formation of martensite reduces the corrosion potential. More importantly, the galvanic effect between austenite and martensite degrades the stability and integrity of passive film. Lv et al. [68,69] demonstrated that inhibiting the strain-induced α′-martensite transformation could ease the galvanic effect and improve the corrosion resistance of stainless steel in borate buffer solution.

In fact, during sandpaper grinding, changes in roughness, grain size, residual strain/stress state and martensitic transformation can occur at the same time. Therefore, the possible effects on corrosion behavior are often a mixture of multiple factors. However, according to the current research, it is confirmed that the corrosion resistance of the materials is significantly reduced after sandpaper grinding, which is mainly due to the formation of martensite and increased residual strain/stress. Electropolishing can eliminate the damaged layer caused by surface grinding. More importantly, it can cause enrichment of Cr on the sample surface, thereby enhancing the passivation. Therefore, the passive film formed on the electropolished surface and contains higher Cr content is thicker than that on the ground surface (Fig. 10). It should be noted that for the ground surface state, only the as-printed sample is able to passivate, suggesting the passivation ability of this sample is more resilient to surface condition.

5. Conclusions

This work systematically investigated the influences of heat treatment and surface state on the corrosion resistance of a LPBF 304L SS containing low Si/Mn in 3.5 wt% NaCl solution. Detailed microstructural analysis was combined with electrochemical testing to provide a comprehensive understanding of the corrosion behavior of this LPBF 304L SS. The main findings are:

(1) Heat treatment impact: Cellular dislocation structure in the as-received LPBF 304L SS can enhance the passivation. However, 1050 °C-0.5 h heat treatment significantly decreases the corrosion resistance (the passive range disappears), mainly due to the disappearance of cellular structure and the presence of residual dislocations/strain. 1200 °C-0.5 h heat treatment slightly enhances the corrosion resistance thanks to the enhancement of {101} texture, formation of Cr-rich inclusion, and further reduction of residual strain.
(2) Surface state impact: The electropolished sample shows higher corrosion resistance than the ground counterpart. This is because electropolishing eliminates the surface deformation layer and induces slight Cr enrichment. In contrast, sandpaper grinding induces high residual stress/strain and martensitic transformation which in turn reduces the stability of passive film. Only the as-received LPBF 304L SS retains the ability to passivate after sandpaper grinding.

Data availability

The raw/processed data required to reproduce these findings cannot be shared at this time as the data also forms part of an ongoing study.

Declaration of competing interest

The authors declare that they have no known competing financial interests or personal relationships that could have appeared to influence the work reported in this paper.

Acknowledgments

The authors gratefully acknowledge the financial support of National Natural Science Foundation of China (No. 52271068), Development Program of the Ministry of Science and Technology of China (No. 2019YFA0209900) and Young Talent Support Plan of Xi'an Jiaotong University. The authors thank Research Fellow Wei Wang, Shengwu Guo and Yanhuai Li of Xi'an Jiaotong University for their help of SEM, TEM and XRD characterization, Chenyu Liang at Instrument Analysis Center of Xi'an Jiaotong University for her help on XPS characterization, and Chaowei Guo at Center for Advancing Materials Performance from the Nanoscale (CAMP-Nano) of Xi'an Jiaotong University for their assistance with SEM analysis. The authors would like to thank Qiao Liu and Shaojun Wu of Xi'an Jiaotong University for their assistance with the experiments.

Appendix A. Supplementary data

Supplementary data to this article can be found online at https://doi.org/10.1016/j.jmrt.2024.03.025.

References

[1] Ngo TD, Kashani A, Imbalzano G, Nguyen KTQ, Hui D. Additive manufacturing (3D printing): a review of materials, methods, applications and challenges. Composites Part B 2018;143:172–96.
[2] DebRoy T, Wei HL, Zuback JS, Mukherjee T, Elmer JW, Milewski JO, Beese AM, Wilson-Heid A, De A, Zhang W. Additive manufacturing of metallic components - process, structure and properties. Prog Mater Sci 2018;92:112–224.
[3] Hou J, Chen W, Chen Z, Zhang K, Huang A. Microstructure, tensile properties and mechanical anisotropy of selective laser melted 304L stainless steel. J Mater Sci Technol 2020;48:63–71.
[4] Wu H, Fan G. An overview of tailoring strain delocalization for strength-ductility synergy. Prog Mater Sci 2020;113:100675.
[5] Frazier WE. Metal additive manufacturing: a review. J Mater Eng Perform 2014;23 (6):1917–28.
[6] Sun C, Wang Y, McMurtrey MD, Jerred ND, Liou F, Li J. Additive manufacturing for energy: a review. Appl Energy 2021;282:116041.
[7] Yap CY, Chua CK, Dong ZL, Liu ZH, Zhang DQ, Loh LE, Sing SL. Review of selective laser melting: materials and applications. Appl Phys Rev 2015;2(4):21.
[8] Gu D, Hagedorn Y-C, Meiners W, Meng G, Batista RJS, Wissenbach K, Poprawe R. Densification behavior, microstructure evolution, and wear performance of selective laser melting processed commercially pure titanium. Acta Mater 2012;60 (9):3849–60.
[9] Wu AS, Brown DW, Kumar M, Gallegos GF, King WE. An experimental investigation into additive manufacturing-induced residual stresses in 316L stainless steel. Metall Mater Trans A 2014;45(13):6260–70.
[10] Zhang S, Wang S, Feng X, Ning Z, Hou J, Kuang W. Insights into the stress corrosion cracking resistance of a selective laser melted 304L stainless steel in high-temperature hydrogenated water. Acta Mater 2022:118561.
[11] Kong DC, Dong CF, Ni XQ, Zhang L, Yao JZ, Man C, Cheng XQ, Xiao K, Li XG. Mechanical properties and corrosion behavior of selective laser melted 316L stainless steel after different heat treatment processes. J Mater Sci Technol 2019;35 (7):1499–507.
[12] Kong D, Dong C, Wei S, Ni X, Zhang L, Li R, Wang L, Man C, Li X. About metastable cellular structure in additively manufactured austenitic stainless steels. Addit Manuf 2021;38:101804.
[13] Trelewicz JR, Halada GP, Donaldson OK, Manogharan G. Microstructure and corrosion resistance of laser additively manufactured 316L stainless steel. J Occup Med 2016;68(3):850–9.
[14] Laleh M, Sadeghi E, Revilla RI, Chao Q, Haghdadi N, Hughes AE, Xu W, De Graeve I, Qian M, Gibson I, Tan MY. Heat treatment for metal additive manufacturing. Prog Mater Sci 2023;133:101051.
[15] Chao Q, Cruz V, Thomas S, Birbilis N, Collins P, Taylor A, Hodgson PD, Fabijanic D. On the enhanced corrosion resistance of a selective laser melted austenitic stainless steel. Scripta Mater 2017;141:94–8.
[16] Hemmasian Ettefagh A, Guo S. Electrochemical behavior of AISI316L stainless steel parts produced by laser-based powder bed fusion process and the effect of post annealing process. Addit Manuf 2018;22:153–6.
[17] Sander G, Tan J, Balan P, Gharbi O, Feenstra DR, Singer L, Thomas S, Kelly RG, Scully JR, Birbilis N. Corrosion of additively manufactured alloys: a review. Corrosion 2018;74(12):1318–50.
[18] Revilla RI, Van Calster M, Raes M, Arroud G, Andreatta F, Pyl L, Guillaume P, De Graeve I. Microstructure and corrosion behavior of 316L stainless steel prepared using different additive manufacturing methods: a comparative study bringing insights into the impact of microstructure on their passivity. Corrosion Sci 2020; 176:108914.
[19] Lin KJ, Gu DD, Xi LX, Yuan LH, Niu SQ, Lv P, Ge Q. Selective laser melting processing of 316L stainless steel: effect of microstructural differences along building direction on corrosion behavior. Int J Adv Manuf Technol 2019;104(5–8): 2669–79.
[20] Sander G, Babu AP, Gao X, Jiang D, Birbilis N. On the effect of build orientation and residual stress on the corrosion of 316L stainless steel prepared by selective laser melting. Corrosion Sci 2021;179:109149.
[21] Song M, Wang M, Lou X, Rebak RB, Was GS. Radiation damage and irradiation-assisted stress corrosion cracking of additively manufactured 316L stainless steels. J Nucl Mater 2019;513:33–44.
[22] Tuo LF, Zhou GS, Yu ZQ, Kang XT, Wang BW. Extrusion process of 304L H-shaped stainless steel used in passive residual heat removal heat exchanger. Nucl Sci Tech 2019;30(4).
[23] Yeh CP, Tsai KC, Huang JY. Effects of relative humidity on crevice corrosion behavior of 304L stainless-steel nuclear material in a chloride environment. Metals 2019;9(11):1185.
[24] Suresh G, Mudali UK, Raj B. Corrosion monitoring of type 304L stainless steel in nuclear near-high level waste by electrochemical noise. J Appl Electrochem 2011; 41(8):973–81.
[25] Yang F, Zhu D, Jiang M, Liu H, Guo S, Wang Q, Wang H, Zhang K, Huang A, Hou J. Effect of heat treatment on the microstructure, mechanical properties and corrosion resistance of selective laser melted 304L stainless steel. Acta Metall Sin (Engl Lett) 2022;35(10):1688–702.
[26] Voisin T, Forien J-B, Perron A, Aubry S, Bertin N, Samanta A, Baker A, Wang YM. New insights on cellular structures strengthening mechanisms and thermal stability of an austenitic stainless steel fabricated by laser powder-bed-fusion. Acta Mater 2021;203:116476.
[27] Kong DC, Dong CF, Ni XQ, Zhang L, Luo H, Li RX, Wang L, Man C, Li XG. The passivity of selective laser melted 316L stainless steel. Appl Surf Sci 2020;504:12.
[28] Ettefagh AH, Guo S. Electrochemical behavior of AISI316L stainless steel parts produced by laser-based powder bed fusion process and the effect of post annealing process. Addit Manuf 2018;22:153–6.
[29] Laleh M, Hughes AE, Xu W, Cizek P, Tan MY. Unanticipated drastic decline in pitting corrosion resistance of additively manufactured 316L stainless steel after high-temperature post-processing. Corrosion Sci 2020;165:108412.
[30] Wang XY, Li DY. Mechanical and electrochemical behavior of nanocrystalline surface of 304 stainless steel. Electrochim Acta 2002;47(24):3939–47.
[31] Balusamy T, Sankara Narayanan TSN, Ravichandran K, Park IS, Lee MH. Influence of surface mechanical attrition treatment (SMAT) on the corrosion behaviour of AISI 304 stainless steel. Corrosion Sci 2013;74:332–44.
[32] Kong D, Ni X, Dong C, Zhang L, Man C, Yao J, Xiao K, Li X. Heat treatment effect on the microstructure and corrosion behavior of 316L stainless steel fabricated by selective laser melting for proton exchange membrane fuel cells. Electrochim Acta 2018;276:293–303.
[33] Sander G, Thomas S, Cruz V, Jurg M, Birbilis N, Gao X, Brameld M, Hutchinson CR. On the corrosion and metastable pitting characteristics of 316L stainless steel produced by selective laser melting. J Electrochem Soc 2017;164(6):C250–7.
[34] Yin Y, Li H, Pan S, Zhang J, Han Q, Yang S. Electrochemical behaviour of passivation film formed on SLM-fabricated Hastelloy X superalloy surface in 10 wt % NaNO3 solution. Corrosion Sci 2022;206:110494.
[35] Kong D, Ni X, Dong C, Lei X, Zhang L, Man C, Yao J, Cheng X, Li X. Bio-functional and anti-corrosive 3D printing 316L stainless steel fabricated by selective laser melting. Mater Des 2018;152:88–101.
[36] Mu J, Sun T, Leung CLA, Oliveira JP, Wu Y, Wang H, Wang H. Application of electrochemical polishing in surface treatment of additively manufactured structures: a review. Prog Mater Sci 2023;136:101109.
[37] Chang L, Volpe L, Wang YL, Burke MG, Maurotto A, Tice D, Lozano-Perez S, Scenini F. Effect of machining on stress corrosion crack initiation in warm-forged type 304L stainless steel in high temperature water. Acta Mater 2019;165:203–14.
[38] Chang L, Burke MG, Scenini F. Understanding the effect of surface finish on stress corrosion crack initiation in warm-forged stainless steel 304L in high-temperature water. Scripta Mater 2019;164:1–5.
[39] Chang L, Burke MG, Scenini F. Stress corrosion crack initiation in machined type 316L austenitic stainless steel in simulated pressurized water reactor primary water. Corrosion Sci 2018;138:54–65.
[40] Deng P, Yin H, Song M, Li D, Zheng Y, Prorok BC, Lou X. On the thermal stability of dislocation cellular structures in additively manufactured austenitic stainless steels: roles of heavy element segregation and stacking fault energy. J Occup Med 2020;72(12):4232–43.
[41] Legros M, Dehm G, Arzt E, Balk TJ. Observation of giant diffusivity along dislocation cores. Science 2008;319(5870):1646–9.
[42] Man C, Dong C, Liu T, Kong D, Wang D, Li X. The enhancement of microstructure on the passive and pitting behaviors of selective laser melting 316L SS in simulated body fluid. Appl Surf Sci 2019;467–468:193–205.
[43] Barbucci A, Cerisola G, Cabot PL. Effect of cold-working in the passive behavior of 304 stainless steel in sulfate media. J Electrochem Soc 2002;149(12):B534–42.
[44] Peguet L, Malki B, Baroux B. Influence of cold working on the pitting corrosion resistance of stainless steels. Corrosion Sci 2007;49(4):1933–48.
[45] Lv JL, Guo WL, Liang TX. The effect of pre-deformation on corrosion resistance of the passive film formed on 2205 duplex stainless steel. J Alloys Compd 2016;686: 176–83.
[46] Monrrabal G, Bautista A, Guzman S, Gutierrez C, Velasco F. Influence of the cold working induced martensite on the electrochemical behavior of AISI 304 stainless steel surfaces. J Mater Res Technol 2019;8(1):1335–46.
[47] Nishihara Y, Nakajima Y, Akashi A, Tsujino N, Takahashi E, Funakoshi K, Higo Y. Isothermal compression of face-centered cubic iron. Am Mineral 2012;97(8–9): 1417–20.
[48] Zhang LN, Szpunar JA, Dong JX, Ojo OA, Wang X. Dependence of crystallographic orientation on pitting corrosion behavior of Ni-Fe-Cr alloy 028. Metall Mater Trans B 2018;49(3):919–25.
[49] Ryan MP, Williams DE, Chater RJ, Hutton BM, McPhail DS. Why stainless steel corrodes. Nature 2002;415(6873):770–4.
[50] Zhou C, Hu S, Shi Q, Tao H, Song Y, Zheng J, Xu P, Zhang L. Improvement of corrosion resistance of SS316L manufactured by selective laser melting through subcritical annealing. Corrosion Sci 2020;164:108353.
[51] Choudhary S, Cruz V, Pandey A, Thomas S, Birbilis N. Element-resolved electrochemical analysis of the passivity of additively manufactured stainless steel 316L. Corrosion Sci 2021;189:109576.
[52] Deng P, Karadge M, Rebak RB, Gupta VK, Prorok BC, Lou X. The origin and formation of oxygen inclusions in austenitic stainless steels manufactured by laser powder bed fusion. Addit Manuf 2020;35:101334.
[53] Yan F, Xiong W, Faierson E, Olson GB. Characterization of nano-scale oxides in austenitic stainless steel processed by powder bed fusion. Scripta Mater 2018;155: 104–8.
[54] Lou X, Andresen PL, Rebak RB. Oxide inclusions in laser additive manufactured stainless steel and their effects on impact toughness and stress corrosion cracking behavior. J Nucl Mater 2018;499:182–90.
[55] Wang K, Chao Q, Annasamy M, Hodgson PD, Thomas S, Birbilis N, Fabijanic D. On the pitting behaviour of laser powder bed fusion prepared 316L stainless steel upon post-processing heat treatments. Corrosion Sci 2022;197:110060.
[56] Duan Z, Man C, Dong C, Cui Z, Kong D, wang L, Wang X. Pitting behavior of SLM 316L stainless steel exposed to chloride environments with different aggressiveness: pitting mechanism induced by gas pores. Corrosion Sci 2020;167: 108520.

[57] Hemmasian Ettefagh A, Guo S, Raush J. Corrosion performance of additively manufactured stainless steel parts: a review. Addit Manuf 2021;37:101689.
[58] Zhang Z, Zhao Z, Li X, Wang L, Liu B, Bai P. Effect of heat treatments on metastable pitting of 316L stainless steel fabricated by selective laser melting. J Mater Res Technol 2022;21:1903–14.
[59] Laleh M, Hughes AE, Xu W, Gibson I, Tan MY. A critical review of corrosion characteristics of additively manufactured stainless steels. Int Mater Rev 2021;66 (8):563–99.
[60] Ralston KD, Birbilis N. Effect of grain size on corrosion: a review. Corrosion 2010; 66(7):075005.
[61] Wang XY, Li DY. Mechanical, electrochemical and tribological properties of nano-crystalline surface of 304 stainless steel. Wear 2003;255(7):836–45.
[62] Bedmar J, García-Rodríguez S, Roldán M, Torres B, Rams J. Effects of the heat treatment on the microstructure and corrosion behavior of 316 L stainless steel manufactured by Laser Powder Bed Fusion. Corrosion Sci 2022;209:110777.
[63] Ghosh S, Kumar MK, Kain V. High temperature oxidation behavior of AISI 304L stainless steel—effect of surface working operations. Appl Surf Sci 2013;264: 312–9.
[64] Prevey PSJAI. ASM handbook. X-ray diffraction residual stress techniques 1986;10: 380–92.
[65] Salim ET, Ismail RA, Halbos HT. Growth of Nb2O5 film using hydrothermal method: effect of Nb concentration on physical properties. Mater Res Express 2019; 6(11):116429.
[66] Schaller RF, Mishra A, Rodelas JM, Taylor JM, Schindelholz EJ. The role of microstructure and surface finish on the corrosion of selective laser melted 304L. J Electrochem Soc 2018;165(5):C234–42.
[67] Liu EY, Zhang YX, Zhu LF, Zeng ZX, Gao RP. Effect of strain-induced martensite on the tribocorrosion of AISI 316L austenitic stainless steel in seawater. RSC Adv 2017;7(71):44923–32.
[68] Lv J, Luo H, Liang T, Guo W. The effects of grain refinement and deformation on corrosion resistance of passive film formed on the surface of 304 stainless steels. Mater Res Bull 2015;70:896–907.
[69] Lv J, Liang T, Wang C, Dong L. Effect of ultrafine grain on tensile behaviour and corrosion resistance of the duplex stainless steel. Mater Sci Eng C 2016;62:558–63.